The Journal of Chemical Physics

Effect of fluids on the critical energy release rate of typical components in shale and andesite by molecular simulations

Cite as: J. Chem. Phys. **157**, 044701 (2022); https://doi.org/10.1063/5.0090157
Submitted: 03 March 2022 • Accepted: 24 June 2022 • Accepted Manuscript Online: 27 June 2022 • Published Online: 01 August 2022

Tianhao Wu and Abbas Firoozabadi

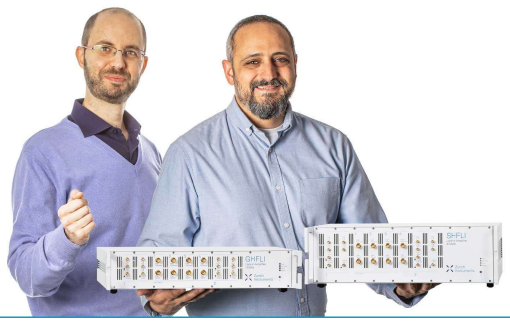

The Journal of Chemical Physics ARTICLE scitation.org/journal/jcp

Effect of fluids on the critical energy release rate of typical components in shale and andesite by molecular simulations

Cite as: J. Chem. Phys. 157, 044701 (2022); doi: 10.1063/5.0090157
Submitted: 3 March 2022 • Accepted: 24 June 2022 •
Published Online: 1 August 2022

Tianhao Wu[1,a] and Abbas Firoozabadi[1,2,b]

AFFILIATIONS

[1] Department of Chemical and Biomolecular Engineering, Rice University, Houston, Texas 70057, USA
[2] Reservoir Engineering Research Institute, Palo Alto, California 94301, USA

[a] **Present address:** School of Environmental Science and Engineering, Southern University of Science and Technology, Shenzhen 518055, People's Republic of China.
[b] **Author to whom correspondence should be addressed:** abbas.firoozabadi@rice.edu

ABSTRACT

The critical energy release rate (G_c) is a key parameter in numerical simulations of hydraulic fracturing, which may be affected by a fluid. Molecular dynamics (MD) simulations of minerals' tensile failure can be performed to gain insights into the mechanisms relevant to the critical energy release rate at the microscale. The methodology of calculating the critical energy release rate for solid–fluid systems is challenging. In this study, we conduct extensive MD simulations for solid–vacuum and solid–fluid systems. Typical components in shale and andesite, including quartz, muscovite, and kerogen, are selected in our investigation. The effect of H_2O and CO_2 on the critical energy release rate is analyzed. Fracture propagation and fluid invasion in fractures are also monitored. The results show that quartz and muscovite are brittle in H_2O and CO_2 and kerogen has very pronounced ductile behavior. H_2O can reduce the critical energy release rate of quartz and muscovite slightly, but may increase that of kerogen. The effect of CO_2 on quartz and muscovite is mild, while it reduces G_c of kerogen significantly. The implication is the creation of a much higher surface area in kerogen by CO_2 than by H_2O, which is in line with large-scale observations.

I. INTRODUCTION

Hydraulic fracturing is a key technique in subsurface energy development, including unconventional oil and gas (e.g., shale formations) and geothermal energy (e.g., andesite formations) production.[1,2] Hydraulic fracturing by water is the most common technique due to its low-cost and wide availability.[3] However, an enormous amount of water is required in conventional hydraulic fracturing. The flow-back wastewater contains toxic chemical additives, which pose a potential threat to the environment.[4] The water-free fracturing fluids have been proposed to improve the fracturing effectiveness and environmental stewardship. Various advantages, including lower fracturing pressure, higher fracture intensity, and lower sensitivity of formation, make CO_2 fracturing a promising technique.[5–8]

In hydraulic fracturing, tensile failures are ubiquitous.[9] The ability to resist fracture propagation is characterized as the fracture toughness of a material. From the view of energy, it is often described by the critical energy release rate G_c, which is expressed as the critical value of the stored strain energy (per unit area of newly created surface) released at the time of fracture propagation.[10,11] The critical energy release rate is attributed to the work done in the creation of new surfaces by rupture either in the form of fractures or expansion of the surface area. In numerical simulations of fracturing, G_c is a key parameter in the phase-field method for calculating breakdown pressure and simulating fracture propagation.[12–14] The experimental methods suggested by the International Society of Rock Mechanics (ISRM) are generally used to measure the fracture toughness of rock samples.[15–19] Based on the theories of Griffith[20,21] and Irwin,[11,22,23] G_c can also be approximated through surface energy for brittle materials when the experimental data are not available.

Generally, rocks consist of mineral grains and organic matters, which can lead to significant heterogeneity at the microscale.[24] The

properties of micro-components can affect the macro-properties of the rock. To gain insights at the microscale, molecular dynamics (MD) simulations can be a powerful tool in advancing the understanding of the microscopic mechanisms of the evolution of mechanical properties. There have been extensive studies by MD simulations for tensile failure in typical minerals. The comparative study of phase-field simulations and MD simulations for aragonite failure has shown that the parameters from these two methods are in good agreement.[25] Extensive molecular simulations of tensile failure in silica, illite, and porous carbon were performed by Hantal *et al.*[26] and Brochard *et al.*[27] The relationships between fracture length and critical stress, as well as the critical energy release rate, are also discussed. Complex behaviors have been found in composite materials composed of porous carbon and clay.[28,29] The interface bond density and heterogeneity show a pronounced effect on the failure process. Kerogen is a key component in organic-rich shale. The mechanical properties of kerogen, including Young's modulus, Poisson's ratio, critical energy release rate, and surface energy, have been calculated through MD simulations.[30,31] The results show that the type and maturity of kerogens have a significant effect on the mechanical properties. The failure criterion for kerogen can be described through the failure envelope, which provides the link to macroscopic simulations.

All the above studies on critical energy release rates ignore the fluid effect. The studies are mainly conducted for a bulk solid phase to calculate the critical energy release rate. Solids are generally contacted with fluids in fracturing and reservoir fluids in natural conditions. There have been extensive in-depth studies about the adsorption behavior of CO_2, light hydrocarbon, and hydrocarbon mixture in shale and kerogen.[32–34] The diffusion of CO_2 and light hydrocarbons in kerogen has been investigated in recent studies.[35–37] The solid–fluid interaction can be very strong. Wu and Firoozabadi[38] discussed the effect of solid–fluid interaction on the interfacial energy of Lennard-Jones solid–fluid systems. Overall, the effect of fluids on the critical energy release rate is largely unknown. The calculation of G_c for solid–fluid systems by MD simulations is challenging.

In this study, the critical energy release rate of typical components in shale and andesite is calculated by MD simulations. The effect of H_2O and CO_2 on the critical energy release rate of quartz, muscovite, and kerogen is investigated. The fracture propagation and fluid invasion in the created fractures are monitored.

II. MATERIAL AND METHODS

A. Molecular model

We select α-quartz to represent a major component in both shale and andesite. The molecular model is presented in Fig. 1. The structure is constructed with 10 × 5 × 12 unit cells of α-quartz.[39] The size of the quartz model is about 5.0 × 2.8 × 10.2 nm^3. A notch with a size of about one unit cell is created to control the direction of fracture propagation consistent with the practice of fracture toughness experiments. For the solid slab, the (001) surface is cut based on the structure in Fig. 1(b). The surface is hydroxylated to generate Q2 surfaces.[39] The notches are at the two sides of the slab surfaces [see Fig. 1(c)]. The quartz–fluid structures are generated based on the quartz slab in Fig. 1(c). Fluid molecules are placed on the two sides of the solid slab [see Figs. 1(d) and 1(e)]. There are 3500 H_2O molecules and 3480 CO_2 molecules in total in quartz–H_2O and quartz–CO_2 systems, respectively.

We select muscovite to represent layered minerals (e.g., mica and clay) in shale and andesite. The molecular model is presented in Fig. 2. The structure is constructed with 24 × 3 × 3 unit cells of muscovite.[40] The size of the muscovite model is about 6.0 × 2.7 × 13.0 nm^3, where the x-direction is rotated to the normal direction of the bedding of the layers. The basic composition is $KAl_2(Si_3Al)O_{10}(OH)_2$. Then, hydrogen or OH group is added to modify the edge atoms. There is no need for notches in the muscovite due to the layered structure. The muscovite–fluid structures are generated based on the muscovite slab in Fig. 2(b). There are 3500 H_2O molecules and 3500 CO_2 molecules placed in the space on the two sides of the muscovite–H_2O and muscovite–CO_2 systems, respectively.

Type II-C kerogen ($C_{242}H_{219}O13N_5S_2$) is selected to represent the organic matter in shale rocks (see Fig. 3). The kerogen macromolecule units are constructed based on the molecular structures from the work of Ungerer *et al.*,[41] which reproduce the elemental and functional data of kerogen. There are 32 kerogen macromolecules in our model. The construction follows the procedures in the work of Wu and Firoozabadi,[42] with the exception that dummy particles are not used. In the final step, a flat graphene sheet is inserted to compress the kerogen matrix to have a relatively flat surface [see Fig. 3(b)]. The size of the kerogen matrix is 4.4 × 4.2 × 9.7 nm^3. The fluid molecules are placed on two sides of the solid slab. There are 5130 H_2O molecules and 5130 CO_2 molecules in total. The size dependency of the bulk kerogen phase was discussed by Wu and Firoozabadi;[31] the system in this study is selected to provide the results independent of size. The size dependency of kerogen–vacuum and kerogen–fluid is also examined.

B. Tensile failure by molecular dynamics simulations

The Large-scale Atomic/Molecular Massively Parallel Simulator (LAMMPS) is applied to perform MD simulations.[43] The Visual Molecular Dynamics (VMD) is used to render the molecular structures.[44] For quartz and muscovite systems, the interactions are described by using the ClayFF model for solid atoms,[45] the Extended Simple Point Charge (SPC/E) model for H_2O,[46] and the Elementary Physical Model 2 (EPM2) for CO_2.[47] The kerogen systems, including H_2O and CO_2, are constructed with polymer consistent force field plus (PCFF+) by using MedeA.[41,48,49] The cut-off for the short-range interactions is set to 12 Å. Long-range interactions are computed by using the particle–particle–particle–mesh (PPPM) method with an accuracy of 1 × 10^{-5}.[50] The periodic boundary condition is applied in all three directions.

We perform two types of simulations: quasi-static and dynamic. Quasi-static simulations are performed to calculate the critical energy release rate, while dynamic simulations are carried out to monitor the tensile failure process and track the flow of the fluids.

Quasi-static simulations are based on a series of strain-driven mechanical processes. In each stage, the stress due to deformation is calculated based on equilibrium simulation, in which the rate effect of deformation is eliminated. The procedure is the same as the method in the work of Wu and Firoozabadi.[31] A series of small tensile strains are applied in the x-direction; the dimension in the y-direction is kept constant.[21,26,27,29] The pressure in the z-direction

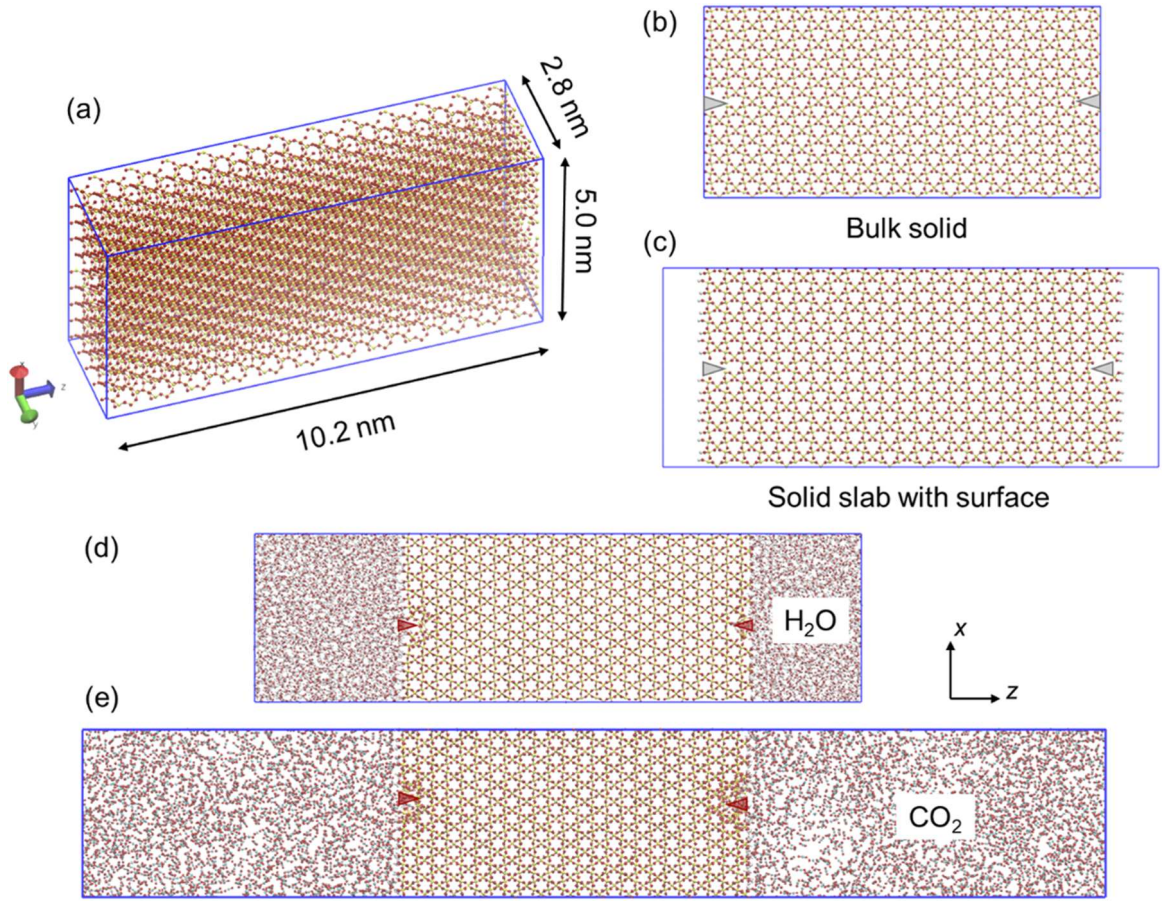

FIG. 1. Molecular model of quartz and quartz–fluid systems. (a) Sketch of the quartz model. (b) Bulk quartz phase with a notch. (c) Quartz slab with hydroxylated surface and notches. (d) Quartz–H_2O system. (e) Quartz–CO_2 system.

is maintained at 10 MPa with the Nose–Hoover barostat to simulate the reservoir conditions of geothermal formations and shale oil/gas reservoirs in a rough range. The strain of each stage is set to 0.5% in quartz and muscovite systems. Because kerogen may take large deformations, the strain of each stage is set to 1.0%. At each stage, the temperature is maintained at 298.15 K by using the Nose–Hoover thermostat. Other temperature conditions are also examined. The simulation time is set to 200 ps for each stage, the last 100 ps of which are used to calculate mechanical properties. The time step is 1 fs. We have compared the simulations with different relaxation times for each stage (200 ps vs 1000 ps) in quartz and quartz–fluid systems, and there is no pronounced difference (see Fig. S1).

Dynamic simulations are based on continuous deformation across the whole time by using non-equilibrium simulations. A rate of deformation in the x-direction is assigned to the whole system. The dimension in the y-direction is kept constant. The pressure in the z-direction is maintained at 10 MPa through the Nose–Hoover barostat. The coordinates of each atom are updated every time step. The deformation rate is about 0.024 ns^{-1} for quartz and muscovite and 0.048 ns^{-1} for kerogen. The temperature is maintained by using the Nose–Hoover thermostat at 298.15 K. The evolution of the average stress is recorded every 200 ps.

C. Calculation of critical energy release rate (G_c) of solid–fluid systems

The total work done for creating the new crack area is equal to the stored strain energy by assuming that the strain energy is completely released after rupture. By integrating the stress–strain curve, G_c is obtained through[26,27,29]

$$G_c = \frac{1}{A_{\text{crack}}}\int_{\text{loading}} Fdl = \frac{V}{A_{\text{crack}}}\int_{\text{loading}} \sigma d\varepsilon, \tag{1}$$

where A_{crack} is the total crack area created in the failure process,[26,27,29] F is the external force, l is the length along the direction of tension, V is the initial volume of the solid, and σ and ε are the stress and strain, respectively. In solid–fluid systems, the stress condition is complex (see Fig. 4). Over the tensile failure process, the stress in the solid (x-direction) can be different from that in the fluid. The overall stress of the whole system is a function of the stresses in

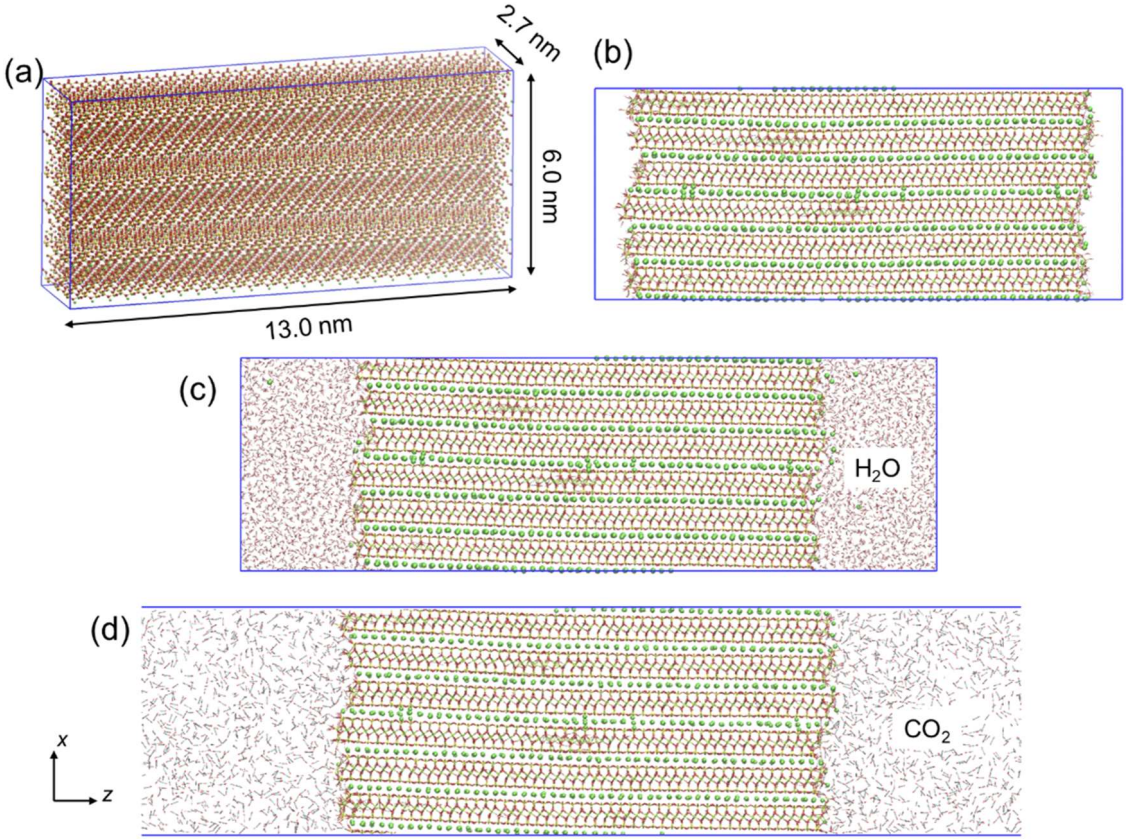

FIG. 2. Molecular model of muscovite and muscovite–fluid systems. (a) Sketch of the muscovite model. (b) Muscovite slab in vacuum. (c) Muscovite–H_2O system. (d) Muscovite–CO_2 system. The main part of the domain is shown in (d).

solid and fluid phases and the interfacial tension. The calculation of the stress for the whole system is well defined, but the calculation of the local stress in a certain region (solid) for such complex systems is challenging. Therefore, the stress–strain relationship in the solid phase cannot be obtained accurately. However, the work of the "whole" solid–fluid system can be estimated by using the overall stress and displacement. The pressure of the fluid phase is kept constant, and we assume that the volume of the fluid phase does not have appreciable change. As a result, the work done on the fluid phase can be assumed to be zero. All the work done can be attributed to the solid phase, and G_c can be estimated through

$$\begin{aligned} G_c &= \frac{W_T}{A_{\text{crack}}} = \frac{W_x + W_z}{A_{\text{crack}}} \\ &= \frac{\int \sigma_x A_{yz} dl_x + \int \sigma_z A_{xy} dl_z}{A_{\text{crack}}} \\ &= \frac{\sum_{i=1}^{i=N} (\sigma_{x,i} A_{yz,i} \Delta l_{x,i} + \sigma_{z,i} A_{xy,i} \Delta l_{z,i})}{A_{\text{crack}}}, \end{aligned} \tag{2}$$

where W, A, and l are the work, cross-sectional area, and length of the whole system; the subscript T in W_T denotes the total work; x, y, and z are plane indices; and N is the number of stages (small strains) for G_c calculation. The work in the y-direction is zero because the dimension is kept constant. The same also applies in solid–vacuum systems. In brittle materials (e.g., quartz and muscovite), only the stages before the breakdown in the stress–strain curve are used in G_c calculation, where the post-failure stage is not included. In ductile materials (kerogen), the transient ratio of total work over the crack area is monitored, and the minimum value of which is defined as the critical energy release rate. The results are calculated based on at least three parallel simulations.

Note that the crack area A_{crack} is often defined as the projected area of the fracture, which refers to the cross-sectional area of the domain or the crack length multiplied by the thickness of the sample.[10,29] The crack areas of quartz and muscovite follow the conventional definition. In kerogen, because of the complex shape of the created surface, we define A_{crack} as half of the total newly created surface area. The newly created surface area is defined as the surface area change from the initial condition to the final stage. The surface area is calculated by using helium as the probe molecule.[42,51] Based on the above consideration, we use the created surface in kerogen to represent the "fracture" in this study, which is in line with Griffith's theory.[20,21]

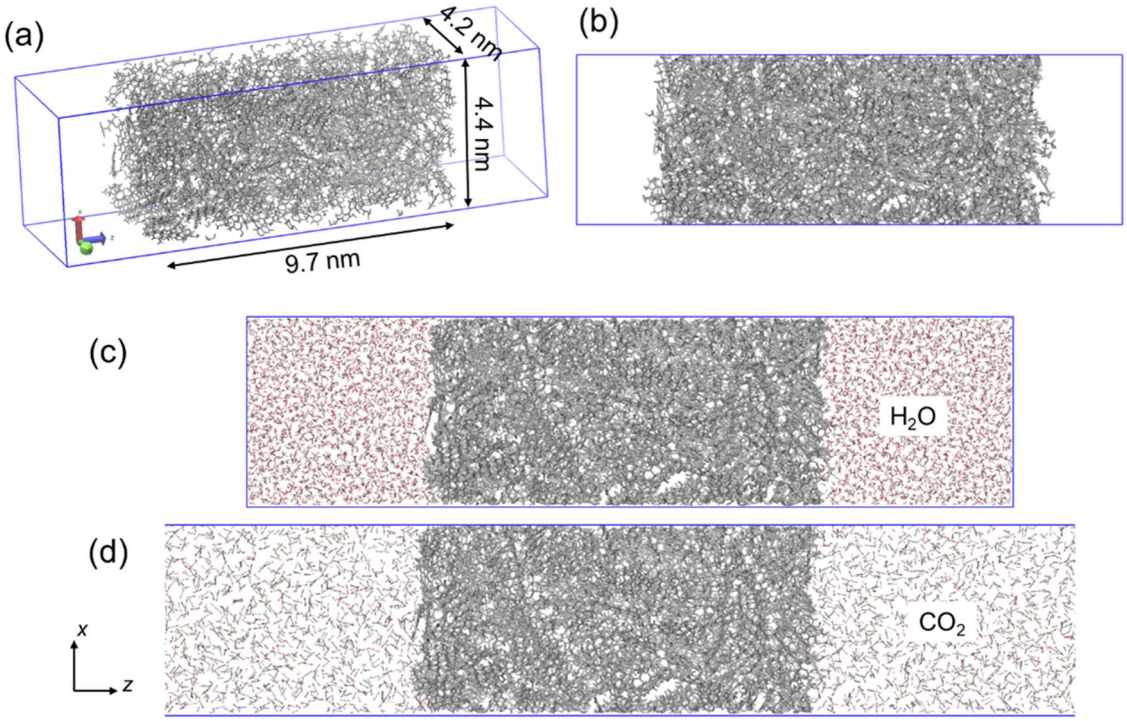

FIG. 3. Molecular model of kerogen and kerogen–fluid systems. (a) Sketch of the kerogen model. (b) Kerogen slab in vacuum. (c) Kerogen–H_2O system. (d) Kerogen–CO_2 system. The main part of the domain is shown in (d).

The critical stress σ_t is often estimated based on the stress–strain relationship in bulk solid (single-phase). However, because of the difficulty in obtaining an accurate stress–strain relationship of the solid phase in solid–fluid systems, the normalized stress of the whole system is provided instead. The stress σ_{xx} is normalized by the maximum stress $\sigma_{xx,\max}$ in each simulation. In this study, we estimate the critical stress for solid–fluid systems through G_c. Generally, the critical stress of a sample with a crack (or notches and defects) length of $2c$ is estimated based on the theories of Griffith and Irwin,[10,21,23,31]

$$\sigma_t = \sqrt{\frac{EG_c}{\pi c}}, \tag{3}$$

where E is Young's modulus. We assume that the notches (or the defects) in the solid are the same in bulk solid and the corresponding

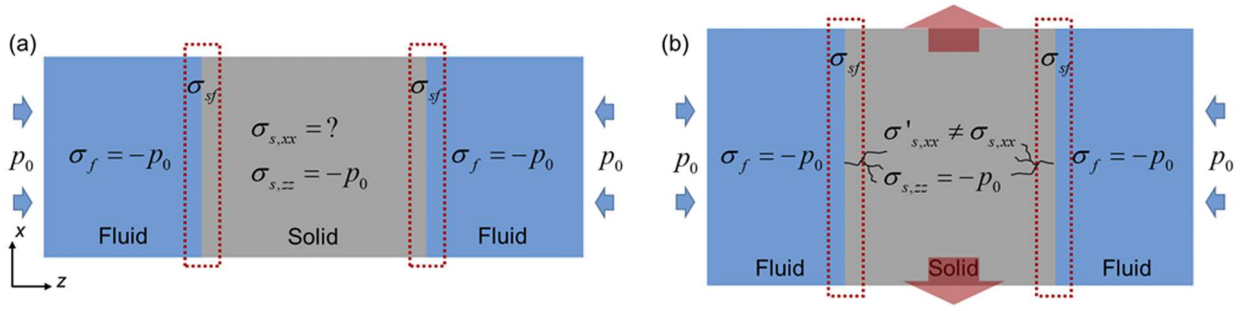

FIG. 4. Sketch of the tensile failure process and the corresponding stress condition. (a) Initial condition. (b) Stress condition after stretching the system in the x-direction. The stress in the solid (x-direction) can be different from that in the fluid. The overall stress of the whole system can also be affected by the interfacial tension. Tensile stress and strain are defined as positive.

solid–fluid or solid–vacuum systems. We, therefore, calculate the critical stress of solid in the solid–vacuum or solid–fluid systems from

$$\sigma_t = \sigma_t^* \sqrt{\frac{G_c}{G_c^*}}, \tag{4}$$

where "*" denotes the parameters in the bulk phase. Without the symbol "*," the parameters refer to solid–fluid or solid–vacuum systems. The assumption is made that the fluid does not affect Young's modulus.

III. RESULTS AND DISCUSSION

A. Quartz and quartz–fluid

The stress–strain relationships for the quartz and quartz–fluid systems are presented in Figs. 5 and 6. There is an abrupt rupture in all the cases. The fractures are created at relatively small strains (<10%). The results indicate that quartz has strong brittleness even in H_2O and CO_2. In dynamic simulations, the speed of H_2O invasion into newly created fractures is much slower than fracture opening. However, the speed of CO_2 invasion is about the same as the fracture opening. When the solid breaks initially, the stress is released

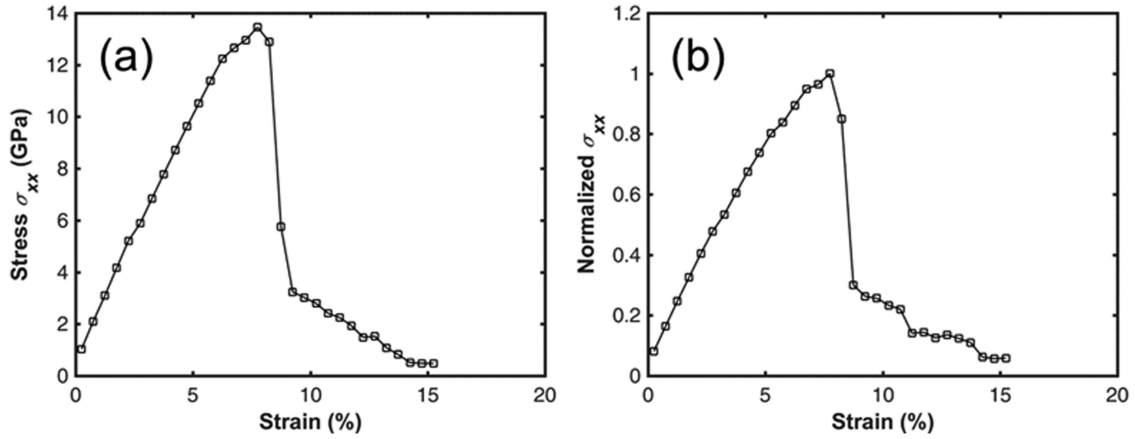

FIG. 5. Tensile stress–strain relationship of quartz by quasi-static simulations. (a) Bulk quartz without surface. (b) Quartz slab in vacuum. The stress σ_{xx} is normalized by the maximum stress $\sigma_{xx,max}$ of the whole system in (b).

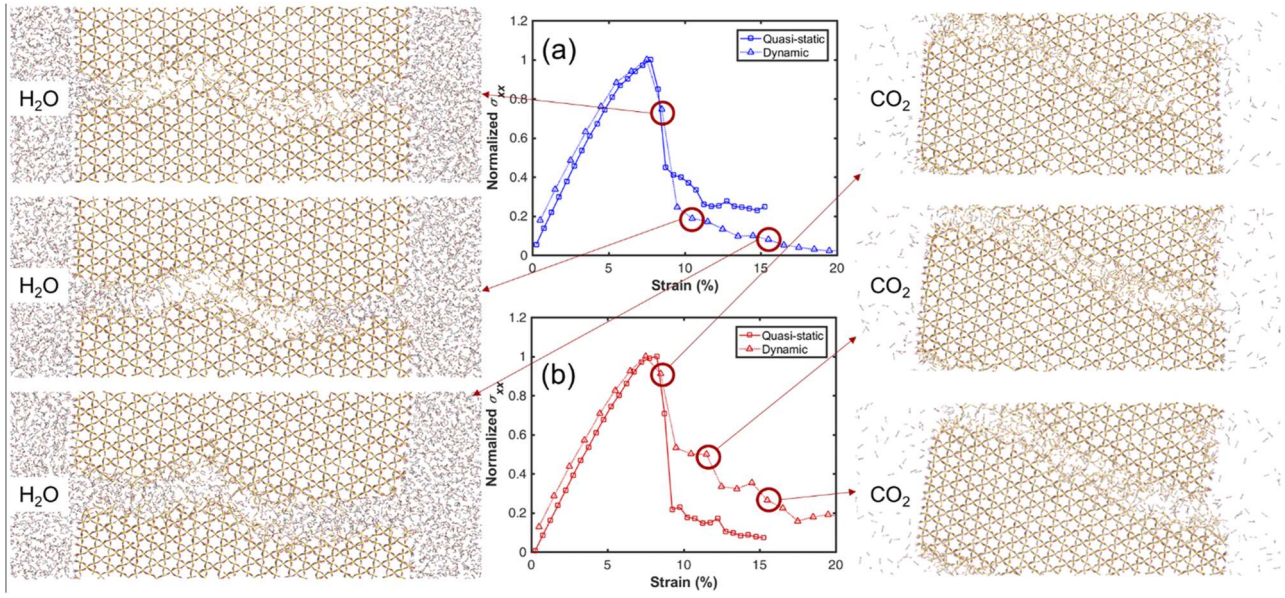

FIG. 6. Stress–strain relationships in (a) quartz–H_2O and (b) quartz–CO_2 systems, and the evolution of H_2O and CO_2 flow in the newly created fracture. The tensile stress–strain relationships are presented in the central panel. The evolution in the post-failure stage is monitored. The fracture is formed within the time scale of 100 ps, which is much faster than H_2O invasion. The speed of CO_2 invasion is about the same as the fracture propagation.

TABLE I. Critical energy release rate (G_c) and critical stress (σ_t) of quartz and quartz–fluid systems.

System	G_c (J/m^2)	σ_t (GPa)
Quartz (bulk)	3.61 ± 0.04	13.11 ± 0.01
Quartz–vacuum	3.48 ± 0.03	12.87 ± 0.05
Quartz–H_2O	3.50 ± 0.05	12.92 ± 0.09
Quartz–CO_2	3.55 ± 0.10	13.00 ± 0.17

immediately, but the fracture is not fully opened to allow for CO_2 invasion. This leaves time for CO_2 to flow into the created fracture in the post-failure stage [see Fig. 6(b) and the right panel]. Different speeds of fluid invasion between H_2O and CO_2 may also result from their different compressibilities. The created fractures in quartz and quartz–fluid systems are represented in Fig. S2, which look similar in these systems. The created surfaces have pronounced zigzags, which follow the pattern of the crystal lattice.

Table I shows the critical energy release rate and the critical stress of quartz and quartz–fluid systems. The results show that the critical energy release rate of quartz is in reasonable agreement with the calculated values by surface energy from experiments.[52] Hydroxylated surface is generally from the interaction with H_2O molecules, but liquid water does not further lower the critical energy release rate, compared with the quartz slab with hydroxylated surfaces in vacuum. Compared with the bulk quartz phase, H_2O reduces the critical energy release rate of quartz by about 10%, including the effect of hydroxylation. The critical stress is also reduced accordingly. The effect of CO_2 on quartz is not appreciable. We have also examined the effect of temperature on G_c. The critical energy release rates of quartz–vacuum and quartz–fluid systems decrease slightly with the increase in temperature. The effect of temperature is not pronounced in the range of 298–573 K (25–300 °C) in our quasi-static simulations (see Fig. S3). The critical energy release rates in quartz–fluid systems at 70 MPa are also calculated. The changes in quartz–H_2O (3.21 J/m^2) and quartz–CO_2 (2.97 J/m^2) systems are not significant.

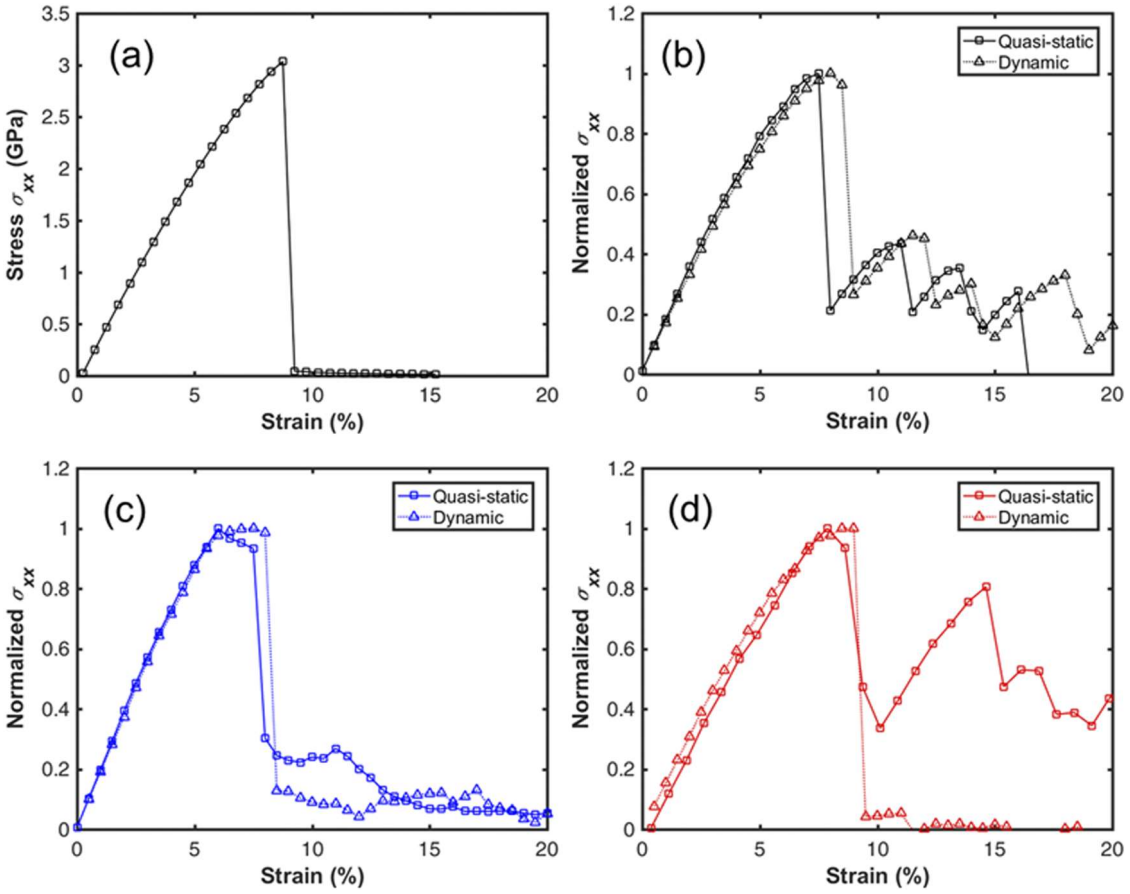

FIG. 7. Tensile stress–strain relationships of muscovite and muscovite–fluid systems by quasi-static and dynamic simulations. (a) Bulk muscovite without surface based on quasi-static simulations. (b) Muscovite slab in vacuum. (c) Muscovite–H_2O system. (d) Muscovite–CO_2 system. The stress σ_{xx} is normalized by the maximum stress $\sigma_{xx,max}$ of the whole system for each plot in (b)–(d).

B. Muscovite and muscovite–fluid

The stress–strain relationships are presented in Fig. 7. The fractures are created at relatively small strains (<10%) with an abrupt rupture. The results indicate that muscovite has strong brittleness in the bulk, vacuum, and in contact with H_2O and CO_2. In quasi-static simulations, the tensile failure mode switches to shear failure in muscovite–vacuum and muscovite–CO_2 systems (see Fig. 8). In the post-failure stage, the stress–strain relationship starts to show zigzags [see Figs. 7(b) and 7(d)]. H_2O can flow into the interlayers and facilitate tensile failure and even multi-interlayer failure [see Fig. 8(b)]. However, CO_2 does not penetrate in quasi-static simulations because shear failure does not create enough space to allow CO_2 to flow into the fracture [see Fig. 8(c)]. Failure results from quasi-static and dynamic simulations are similar in muscovite–vacuum and muscovite–H_2O systems but are different in the muscovite–CO_2 system. CO_2 can invade the interlayer space and maintain tensile failure in dynamic simulations (see Fig. S4). The implication is that the rate of deformation may affect the failure mode due to inertia. The speeds of H_2O and CO_2 invasion into newly created fracture are all slower than fracture propagation due to the fast fracture propagation in the layered structure of muscovite.

The calculated G_c for muscovite and muscovite–fluid systems is given in Table II. The difference between bulk muscovite and muscovite–vacuum systems is from the edges of the layered structure, which can be treated as a defect. H_2O may reduce the critical energy release rate slightly, while there is a minor increase of G_c in CO_2. However, the overall effects of H_2O and CO_2 on muscovite are not significant.

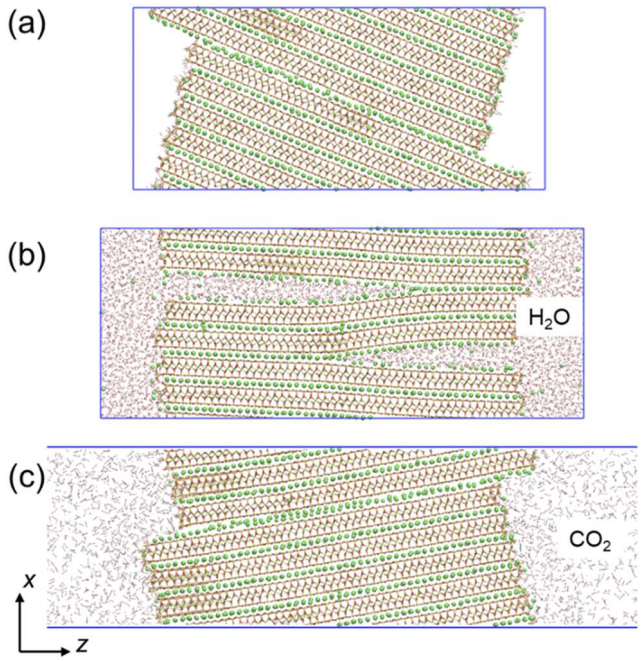

FIG. 8. Created fractures in muscovite and muscovite–fluid systems by quasi-static simulations. (a) Muscovite in vacuum. (b) Muscovite–H_2O system. (c) Muscovite–CO_2 system. In (a) and (c), the failure mode switches to shear failure after tensile failure is observed. H_2O can flow into the interlayers, while CO_2 does not.

TABLE II. Critical energy release rate (G_c) and critical stress (σ_t) of muscovite and muscovite–fluid systems.

System	G_c (J/m^2)	σ_t (GPa)
Muscovite (bulk)	0.98 ± 0.01	2.97 ± 0.01
Muscovite–vacuum	0.71 ± 0.04	2.53 ± 0.07
Muscovite–H_2O	0.64 ± 0.04	2.39 ± 0.08
Muscovite–CO_2	0.78 ± 0.06	2.65 ± 0.10

C. Kerogen and kerogen-fluid

Figure 9 portrays the stress–strain relation for bulk kerogen, kerogen–vacuum, kerogen–H_2O, and kerogen–CO_2 systems. Unlike quartz and muscovite, kerogen can take high strains and have pronounced ductile characteristics. The stress–strain relationships show that the stress reaches the maximum at the strain of 7%–10% and then starts to drop. From the maximum, the stress decreases slowly in kerogen–vacuum and kerogen–H_2O systems but faster in the kerogen–CO_2 system. After the strain of 30%, the overall stress in the kerogen–CO_2 system turns negative. The whole system is under compressive stress, and CO_2 supports the system through fluid pressure instead of the kerogen structure.

The evolution of the structures is presented in Figs. 10, 11, and S5. The solid matrix in the solid–fluid system is not fully separated even at the strain of 130%. By tracing the flow of fluid molecules, we find that H_2O does not penetrate kerogen (Fig. 10), but CO_2 diffuses into the kerogen matrix even at early stages (Fig. 11), which results in different shapes of the created surface in tensile failure (see Fig. 12). The CO_2 distribution in Fig. 11 also supports the compressive stress in Fig. 12(d).

In kerogen–vacuum and kerogen–H_2O systems, the created surfaces often have simple shapes and less surface area. In the kerogen–CO_2 system, the created surfaces are more complex and have higher surface areas. The implication is that fracture intensity in CO_2 fracturing is higher than that in H_2O fracturing in line with various lab-scale observations.[14]

The evolution of the surface area is presented in Fig. 12. The surface area starts to expand before the peak stress, which is from pore space expansion. Then, the surface area increase is higher at the post-failure stage and finally reaches a plateau. The created surface is largely due to the external surface around the two sides, not the pores within the matrix, because the external surface generally has more defects where the crack may initiate. This is also the case for quartz and muscovite. In kerogen, there is no clear edge between the newly created surface and the original external surface because kerogen is ductile and the surfaces are rough. We use the "created surface" instead of a "fracture" to denote this change in kerogen.

The results for the critical energy release rate and critical stress are given in Table III. G_c of the kerogen–vacuum system is 0.39 J/m^2, which is lower than that of the bulk phase because of the defects around the external surface. H_2O may increase the critical energy release rate by 13%, which mainly results from the lower surface area. CO_2 can significantly reduce the critical energy release

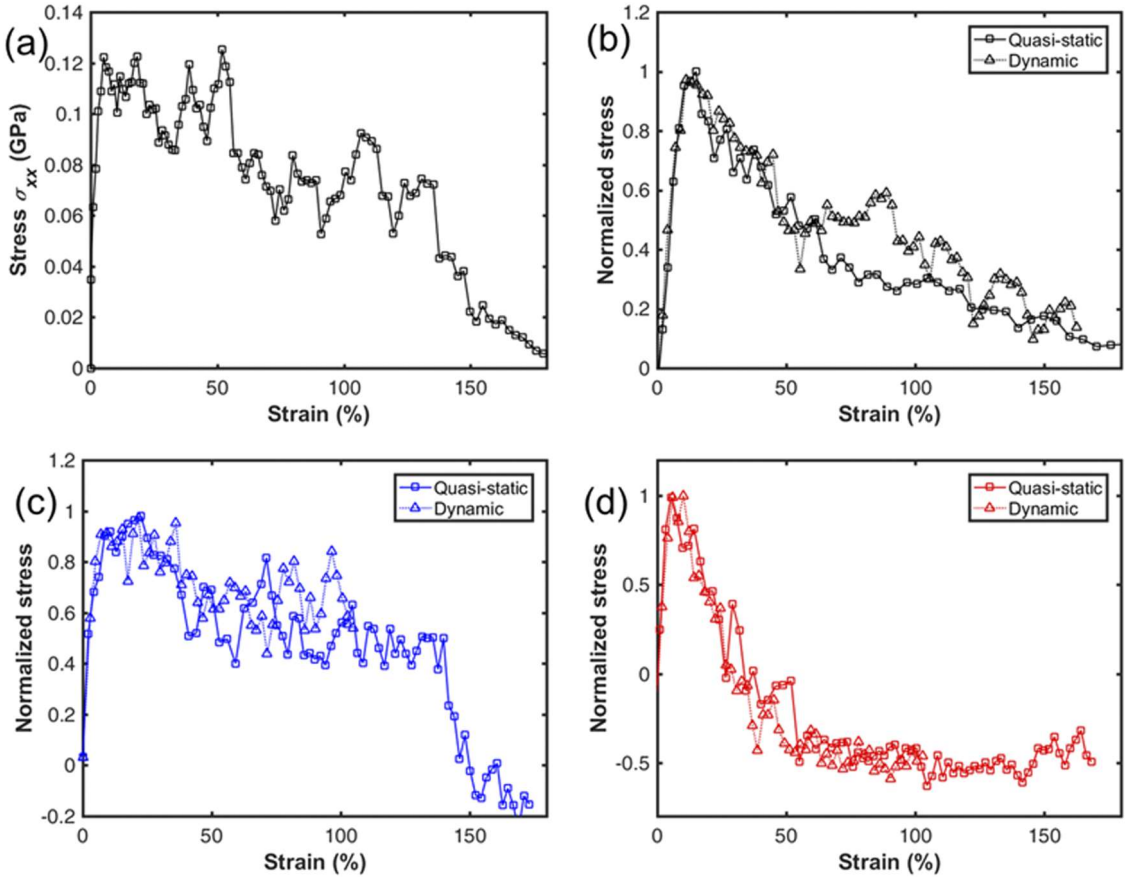

FIG. 9. Tensile stress–strain relationships of kerogen and kerogen–fluid systems by quasi-static and dynamic simulations. (a) Bulk kerogen without surface by quasi-static simulations. (b) Kerogen–vacuum system. (c) Kerogen–H_2O system. (d) Kerogen–CO_2 system. The stress σ_{xx} is normalized by the maximum stress $\sigma_{xx,max}$ of the whole system in each plot from (b)–(d).

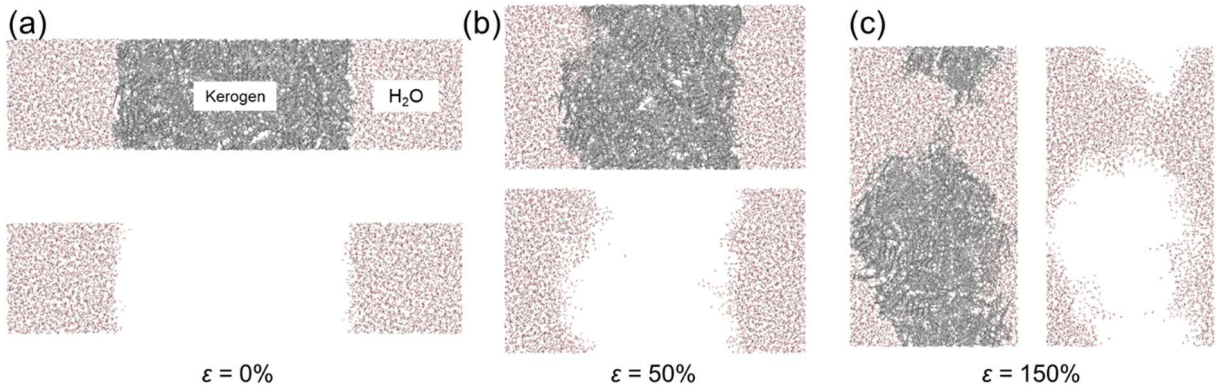

FIG. 10. Evolution of the kerogen–H_2O system at different strains in tensile failure. (a) ε = 0%. (b) ε = 50%. (c) ε = 150%. Kerogen is not shown for tracing the fluid molecules in the lower panel (and right panel at ε = 150%).

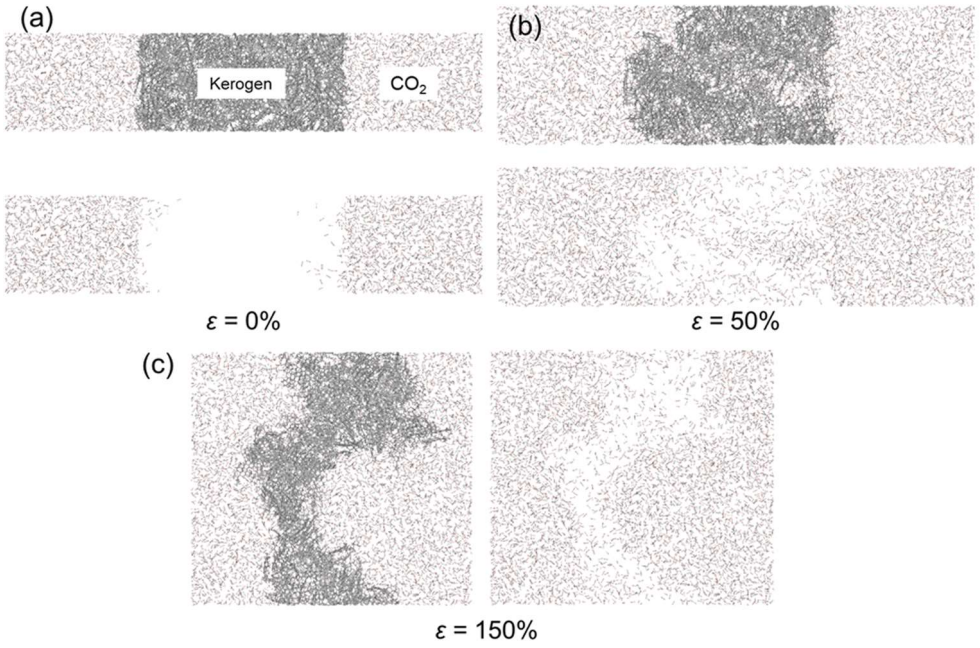

FIG. 11. Evolution of the kerogen–CO_2 system at different strains in tensile failure. (a) ε = 0%. (b) ε = 50%. (c) ε = 150%. Kerogen is not shown for tracing the fluid molecules in the lower panel (and right panel at ε = 150%).

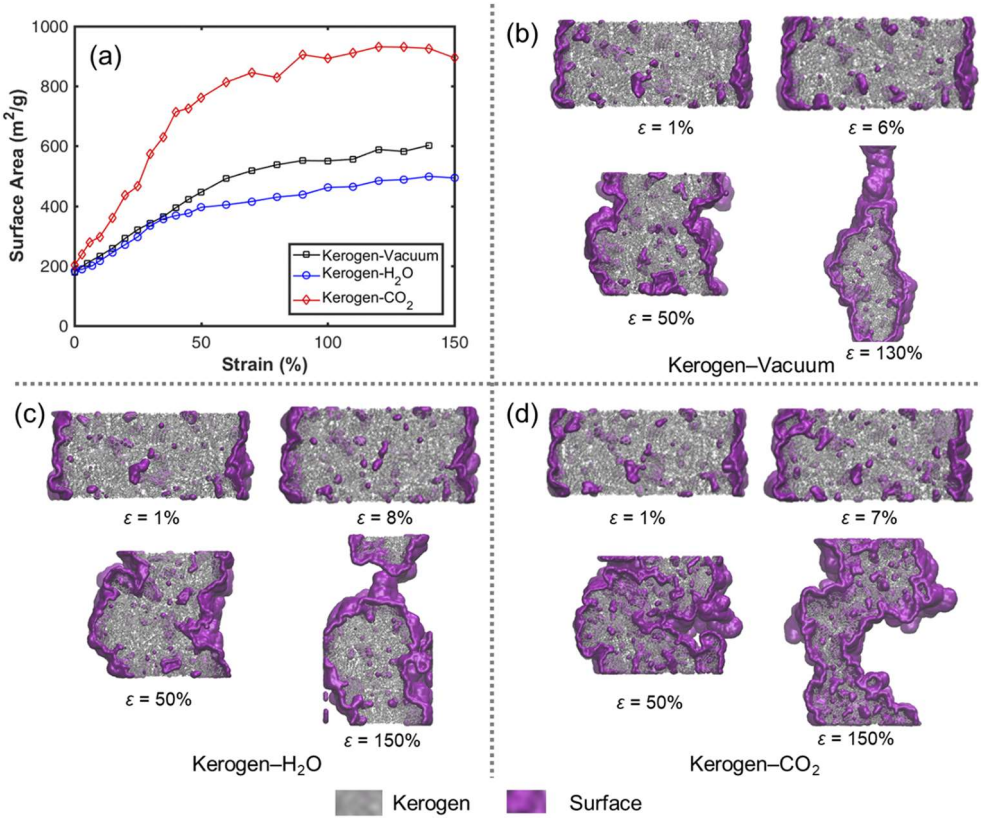

FIG. 12. Evolution of the surface area and morphology of the created surface for kerogen–vacuum and kerogen–fluid systems in tensile failure. The fluid molecules are not shown. The side surfaces are included in the surface area calculation. (a) Surface area evolution. (b) Created surface in the kerogen–vacuum system. (c) Created surface in the kerogen–H_2O system. (d) Created surface in the kerogen–CO_2 system.

TABLE III. Critical energy release rate (G_c) and critical stress (σ_t) of kerogen and kerogen–fluid systems.

System	G_c (J/m^2)	σ_t (GPa)
Kerogen (bulk)	0.55 ± 0.08	0.125 ± 0.004
Kerogen–vacuum	0.39 ± 0.02	0.106 ± 0.002
Kerogen–H_2O	0.44 ± 0.03	0.112 ± 0.004
Kerogen–CO_2	0.10 ± 0.02	0.052 ± 0.005

rate to 0.10 J/m^2, which is a reduction of 74%. The critical stress changes with fluid type, accordingly. It is about 0.112 GPa for the kerogen–H_2O system and 0.052 GPa for the kerogen–CO_2 system. The critical stress of kerogen reduces significantly by CO_2 compared to H_2O.

We have also performed simulations at a higher temperature (373 K) and a higher pressure (70 MPa). The results show that the trend of the fluid effect on G_c in kerogen systems is not changed at a higher temperature and pressure (see Table S1). To verify the results, we have constructed a kerogen matrix with different dimensions (higher length in the z-direction; see Fig. S6). The same number of type II-C kerogen molecules is used to construct the matrix, which follows the same protocol in Sec. II. The results show that the size effect is not appreciable (see Table S1).

IV. CONCLUSIONS

The main conclusions drawn from this study are as follows:

(1) The effect of H_2O and CO_2 on G_c of quartz and muscovite is not appreciable. The hydroxylated surface may reduce the critical energy release rate of quartz by about 10% compared with the bulk quartz.
(2) In kerogen, H_2O may slightly increase the critical energy release rate. CO_2 significantly reduces the critical energy release rate to 0.10 J/m^2, compared to 0.55 and 0.39 J/m^2 in bulk kerogen and kerogen–vacuum systems, respectively.
(3) Critical stress in kerogen is significantly lowered from contact with CO_2. On the other hand, contact with H_2O increases the critical stress mildly. Breakdown pressure in lab-scale hydraulic fracturing in samples of shale by CO_2 and H_2O is consistent with our molecular simulation. The critical energy release rate and critical stress affect the breakdown pressure. The implication is that CO_2 fracturing is a promising technique in shale oil and gas development.
(4) In quartz, the speed of H_2O invasion into the newly created fracture is much lower than fracture opening. The speed of CO_2 invasion is about the same as the fracture opening.
(5) In muscovite, the speeds of H_2O and CO_2 invasion into newly created fracture are lower than fracture propagation. However, CO_2 may not penetrate the shear fractures in quasi-static simulations, but it can invade the interlayer space and create tensile failure in dynamic simulations. The implication is that the rate of deformation may affect the failure mode.
(6) In kerogen, our simulations show the diffusion of CO_2 in the kerogen matrix in the course creation of a new surface area, while we do not observe H_2O diffusion.
(7) We have also conducted molecular simulations on the effect of temperature and pressure on the critical energy release rate G_c of quartz and kerogen systems. We do not observe an appreciable effect of temperature and pressure on G_c in the range of 298–573 K and 10–70 MPa.

SUPPLEMENTARY MATERIAL

See the supplementary material for figures showing the comparison of different relaxation times, the created fractures, and the effect of temperature on the critical energy release rate in quartz and quartz–fluid systems; the evolution of CO_2 flow in muscovite; the evolution of the kerogen–vacuum system at different strains in tensile failure; the evolution of the kerogen–vacuum system at different strains in tensile failure; and the molecular models of kerogen and kerogen–CO_2 systems with different lengths of the kerogen matrix in the z-direction and a table of the critical energy release rate and critical stress of kerogen and kerogen–fluid systems at different temperatures and pressures.

ACKNOWLEDGMENTS

This work was partially supported by the member companies of the Reservoir Engineering Research Institute (RERI). We acknowledge the funding from the ExxonMobil project on CO_2 fracking at Rice University under Agreement No. EM11539.

AUTHOR DECLARATIONS

Conflict of Interest

The authors have no conflicts to disclose.

Author Contributions

Tianhao Wu: Conceptualization (equal); Formal analysis (equal); Investigation (equal); Validation (equal); Writing – original draft (equal). **Abbas Firoozabadi:** Conceptualization (equal); Formal analysis (equal); Funding acquisition (equal); Investigation (equal); Resources (equal); Supervision (equal); Writing – review & editing (equal).

DATA AVAILABILITY

The data that support the findings of this study are available from the corresponding author upon reasonable request.

REFERENCES

[1] EIA, Annual Energy Outlook 2019: With Projections to 2050, 2019, available at: https://www.eia.gov/outlooks/archive/aeo19/.
[2] EIA, Technically recoverable shale oil and shale gas resources, 2013, available at: https://www.eia.gov/analysis/studies/worldshalegas/.
[3] R. S. Middleton, J. W. Carey, R. P. Currier, J. D. Hyman, Q. Kang, S. Karra, J. Jiménez-Martínez, M. L. Porter, and H. S. Viswanathan, Appl. Energy **147**, 500 (2015).
[4] L. Gandossi, European Commission Jt. Res. Cent. Technical Report No. 26347, 2013.

[5]H. Liu, F. Wang, J. Zhang, S. Meng, and Y. Duan, Pet. Explor. Dev. **41**, 513 (2014).
[6]M. L. Sinal and G. Lancaster, J. Can. Pet. Technol. **26**, PETSOC-87-05-01 (1987).
[7]T. Wu, J. Zhao, W. Zhang, and D. Zhang, Nano Energy **69**, 104426 (2020).
[8]X. Zhang, Y. Lu, J. Tang, Z. Zhou, and Y. Liao, Fuel **190**, 370 (2017).
[9]S. Li and D. Zhang, SPE J. **24**(02), 857–876 (2018).
[10]T. L. Anderson, *Fracture Mechanics: Fundamentals and Applications* (CRC Press, Boca Raton, 2005).
[11]G. R. Irwin, J. Appl. Mech. **24**, 361 (1957).
[12]Y. Heider, S. Reiche, P. Siebert, and B. Markert, Eng. Fract. Mech. **202**, 116 (2018).
[13]S. Zhou, X. Zhuang, and T. Rabczuk, Comput. Methods Appl. Mech. Eng. **350**, 169 (2019).
[14]Y. Feng, K. Haugen, and A. Firoozabadi, J. Geophys. Res.: Solid Earth **126**, e2021JB022509, https://doi.org/10.1029/2021jb022509 (2021).
[15]M. R. Chandler, P. G. Meredith, N. Brantut, and B. R. Crawford, J. Geophys. Res.: Solid Earth **121**, 1706, https://doi.org/10.1002/2015jb012756 (2016).
[16]H. Wang, F. Zhao, Z. Huang, Y. Yao, and G. Yuan, Rock Mech. Rock Eng. **50**, 1933 (2017).
[17]M. D. Kuruppu, Y. Obara, M. R. Ayatollahi, K. P. Chong, and T. Funatsu, Rock Mech. Rock Eng. **47**, 267 (2014).
[18]R. Fowell, J. Hudson, C. Xu, and X. Zhao, Int. J. Rock Mech. Min. Sci. Geomech. Abstr. **32**, 57–64 (1995).
[19]J. Franklin, S. Zongqi, B. K. Atkinson, P. C. Meredith, F. Rummel, W. Mueller, Y. Nishimatsu, H. Takahahsi, L. S. Costin, A. R. Ingraffea, and G. F. Bobrov, Int. J. Rock Mech. Min. Geomech. Abstr. **25**, 71 (1988).
[20]A. A. Griffith, Philos. Trans. R. Soc., A **221**, 163 (1921).
[21]A. A. Griffith, in Proceedings of the First International Congress for Applied Mechanics (1924), p. 55.
[22]G. R. Irwin, *Fracturing of Metals* (ASM, Cleveland, 1948), p. 147.
[23]G. R. Irwin, in *Elasticity and Plasticity/Elastizität und Plastizität*, edited by S. Flügge (Springer, Berlin, Heidelberg, 1958), p. 551.
[24]T. Wu, X. Li, J. Zhao, and D. Zhang, Water Resour. Res. **53**, 5438, https://doi.org/10.1002/2017wr020780 (2017).
[25]S. P. Patil, Y. Heider, C. A. Hernandez Padilla, E. R. Cruz-Chú, and B. Markert, Comput. Methods Appl. Mech. Eng. **312**, 117 (2016).
[26]G. Hantal, L. Brochard, H. Laubie, D. Ebrahimi, R. J.-M. Pellenq, F.-J. Ulm, and B. Coasne, Mol. Phys. **112**, 1294 (2014).
[27]L. Brochard, G. Hantal, H. Laubie, F.-J. Ulm, and R. J.-M. Pellenq, Int. J. Fract. **194**, 149–167 (2015).
[28]G. Hantal, L. Brochard, M. N. Dias Soeiro Cordeiro, F.-J. Ulm, and R. J.-M. Pellenq, J. Phys. Chem. C **118**, 2429 (2014).
[29]G. Hantal, L. Brochard, R. J.-M. Pellenq, F.-J. Ulm, and B. Coasne, Langmuir **33**, 11457 (2017).
[30]T. Wu and A. Firoozabadi, J. Phys. Chem. C **124**, 2289 (2020).
[31]T. Wu and A. Firoozabadi, J. Phys. Chem. C **124**, 15895 (2020).
[32]T. Wu, H. Zhao, S. Tesson, and A. Firoozabadi, Fuel **235**, 855 (2019).
[33]H. Zhao, T. Wu, and A. Firoozabadi, Fuel **224**, 412 (2018).
[34]Y. Yang, J. Liu, J. Yao, J. Kou, Z. Li, T. Wu, K. Zhang, L. Zhang, and H. Sun, Chem. Eng. J. **387**, 124054 (2020).
[35]A. Obliger, P.-L. Valdenaire, F.-J. Ulm, R. J.-M. Pellenq, and J.-M. Leyssale, J. Phys. Chem. B **123**, 5635 (2019).
[36]S. Wang, X. Yao, Q. Feng, F. Javadpour, Y. Yang, Q. Xue, and X. Li, Chem. Eng. J. **425**, 130292 (2021).
[37]J. Liu, Y. Yang, S. Sun, J. Yao, and J. Kou, Chem. Eng. J. **434**, 134682 (2022).
[38]T. Wu and A. Firoozabadi, J. Phys. Chem. A **125**, 5841 (2021).
[39]F. S. Emami, V. Puddu, R. J. Berry, V. Varshney, S. V. Patwardhan, C. C. Perry, and H. Heinz, Chem. Mater. **26**, 2647 (2014).
[40]S. L. Teich-McGoldrick, J. A. Greathouse, and R. T. Cygan, J. Phys. Chem. C **116**, 15099 (2012).
[41]P. Ungerer, J. Collell, and M. Yiannourakou, Energy Fuels **29**, 91 (2015).
[42]T. Wu and A. Firoozabadi, J. Phys. Chem. C **123**, 10874 (2019).
[43]S. Plimpton, J. Comput. Phys. **117**, 1 (1995).
[44]W. Humphrey, A. Dalke, and K. Schulten, J. Mol. Graphics **14**, 33 (1996).
[45]R. T. Cygan, J.-J. Liang, and A. G. Kalinichev, J. Phys. Chem. B **108**, 1255 (2004).
[46]H. J. C. Berendsen, J. R. Grigera, and T. P. Straatsma, J. Phys. Chem. **91**, 6269 (1987).
[47]J. G. Harris and K. H. Yung, J. Phys. Chem. **99**, 12021 (1995).
[48]M. Yiannourakou, P. Ungerer, B. Leblanc, X. Rozanska, P. Saxe, S. Vidal-Gilbert, F. Gouth, and F. Montel, Oil Gas Sci. Technol. **68**, 977 (2013).
[49]See https://www.materialsdesign.com/ for MedeA, Version 3.0.
[50]R. Hockney and J. Eastwood, *Computer Simulation Using Particles* (Adam Hilger, New York, 1989).
[51]T. Düren, F. Millange, G. Férey, K. S. Walton, and R. Q. Snurr, J. Phys. Chem. C **111**, 15350 (2007).
[52]G. A. Parks, J. Geophys. Res.: Solid Earth **89**, 3997, https://doi.org/10.1029/jb089ib06p03997 (1984).